Comput Visual Sci 4: 21–30 (2001)

Computing and Visualization in Science

Regular article

Adaptivity in 3D image processing

Eberhard Bänsch[1], **Karol Mikula**[2]

[1] Weierstrass Institute for Applied Analysis and Stochastics, Mohrenstr. 39, D-10117 Berlin, Germany
[2] Department of Mathematics, Slovak University of Technology, Radlinského 11, 813 68 Bratislava, Slovakia

Received: 15 December 1999 / Accepted: 8 June 2001

Communicated by: G. Wittum

Abstract. We present an adaptive numerical scheme for computing the nonlinear partial differential equations arising in 3D image multiscale analysis. The scheme is based on a semi-implicit scale discretization and on an adaptive finite element method in 3D-space. Successive coarsening of the computational grid is used for increasing the efficiency of the numerical procedure. L_∞-stability of the semi–discrete scheme is proved and computational results related to 3D nonlinear image filtering are discussed.

1 Introduction

Nonlinear image multiscale analysis is an important task of computer vision. It is related to selective nonlinear filtering, edge detection, enhancement, segmentation and further operations of image processing. With a new development of medical applications, an efficient and robust treating of 3D problems is highly desirable.

The "scaling of the image" is represented by a solution of a nonlinear PDE for which the processed image gives an initial condition. In the last decade such models have been suggested and studied, and in general they are based on degenerate diffusion equations, see for instance [2, 8–11, 15–17, 19]. The multiscale approach has been axiomatized, i.e. derived from "first principles", in [1]. There, it was proved in a rigorous way that the majority of image processing operations can be viewed as solutions of second order degenerate parabolic partial differential equation. In some sense, it summarizes the linear scale space theories, started in the eighties by Witkin and Koenderink and a few decades before by Iijima, as well as the ideas of the so-called "morphological school", see [13, 20–22].

In this paper, we consider the following problem, which is an interesting combination of linear and nonlinear scale space ideas. Let u be the solution of

$$\partial_t b(u) - \nabla(g(|\nabla G_\sigma * u|)\nabla u) = f(u^0 - u) \text{ in } Q_T \equiv I \times \Omega, \tag{1}$$

$$\partial_\nu u = 0 \quad \text{on} \quad I \times \partial\Omega, \tag{2}$$

$$u(0,\cdot) = u^0 \quad \text{in} \quad \Omega, \tag{3}$$

where $\Omega \subset \mathbb{R}^d$, $d = 3$ in our case, is a bounded domain with Lipschitz continuous boundary (in our application Ω is rectangular), $I = [0, T]$ is a scale interval, and

g is a Lipschitz continuous function,

$$g(0) = 1,\ 0 < g(s) \to 0 \quad \text{for} \quad s \to \infty, \tag{4}$$

$$G_\sigma \in C^\infty(\mathbb{R}^d) \text{ is a smoothing kernel, } \int_{\mathbb{R}^d} G_\sigma(x)dx = 1, \tag{5}$$

$G_\sigma(x) \to \delta_x$ for $\sigma \to 0$, where δ_x is the delta distribution, the convergence is understood in the usual sense and

$$\int_{\mathbb{R}^d} |\nabla G_\sigma|^2 dx \le C_\sigma.$$

$$\nabla G_\sigma * u := \int_{\mathbb{R}^d} \nabla_x G_\sigma(x-\xi)\tilde{u}(\xi)d\xi, \tag{6}$$

where $\tilde{u}$ is some extension of u, e.g. by reflection, such that

$$\|\tilde{u}\|_{L^2(\mathbb{R}^d)} \le C\|u\|_{L^2(\Omega)}. \tag{7}$$

b is a strictly increasing continuous function for which (8)

$$b(0) = 0,\ \Gamma \ge b'(s) \ge \gamma > 0, \tag{9}$$

f is a Lipschitz continuous, nondecreasing function with

Lipschitz constant L, $f(0) = 0$, (10)

$$u^0 \in L_\infty(\Omega) \cap V,\ V = W^{1,2}(\Omega). \tag{11}$$

In [6] we have explained the mechanism of selective smoothing process of the model (1)–(3) in case $b(s) \equiv s$. Such an equation has been suggested by Catté, Lions, Morel and Coll and it combines the ideas of linear Gaussian scaling and nonlinear Perona and Malik anisotropic diffusion equation. We have also reported the role of adaptively coarsened 2D finite element computational grids used in the discrete scale steps. In this paper we present a 3D approach to the problem. We use the structure of tetrahedral meshes obtained by the bisection algorithm ([3–5]), which can be backwardly

coarsened in a straightforward way. Using the coarsening criterion as in [6] we remove tetrahedra from the image regions where the gradient of the image intensity function is small. Moreover, we modify the Catté, Lions, Morel and Coll nonlinear diffusion equation by adding a faster diffusion in those parts of the image which are (a-priori) out of interest. Using a small slope of b for such image intensities we speed up the diffusion and thus enhance the grid coarsening. Such effect, together with the opposite, slowing down of the diffusion process depending on the image intensity and/or position in the image, has been suggested and studied in [11]. There, a kind of Jäger–Kačur algorithm is used for the proof of existence of the solution and provides also a numerical scheme. In this paper we consider the nondegenerate case (8)–(9) in which we use a simpler semi-implicit approximation scheme where all nonlinearities are simply treated from the previous discrete scale step. Thus in each discrete scale step we solve a *linear* elliptic equation by a finite element method with decreasing number of elements due to the coarsening.

In Sect. 3 we prove that such a method is L_∞-stable in a semi-discrete setting. In Sect. 4 we discuss in detail the 3D adaptive finite element space discretization and coarsening strategy in 3D. In Sect. 5 we discuss some computational results with artificial as well as real images.

We mention related work by Preusser and Rumpf [18]. There a similar technique is presented. They use trilinear elements on hexahedra and apply the method to flow field visualization.

2 Notation

Let $\Omega \subseteq \mathbb{R}^3$ be a bounded domain. Denote by $(u, v) := \int_\Omega u(x)v(x)dx$ the L^2 inner product for $u, v \in L^2(\Omega)$. $V := W^{1,2}(\Omega)$ is the Sobolev space of L^2-functions with square integrable weak derivatives.

A *triangulation* $\mathcal{T}$ of Ω is a set of (non-degenerate) tetrahedra with $\bigcup_{T\in\mathcal{T}} T = \bar{\Omega}$.

A triangulation $\mathcal{T}$ is called *conforming* if the intersection of two non-disjoint, non-identical tetrahedra consists either of a common vertex, a common edge or a common face. $T \in \mathcal{T}$ is said to have a *non-conforming node*, if there is a vertex P of the triangulation which is not a vertex of T but $P \in T$. A sequence of triangulations $\mathcal{T}_1, \mathcal{T}_2, \ldots$ has the property of *shape regularity* if $\sup_{T\in\mathcal{T}_k, k\in\mathbb{N}} \{h_T/\rho(T)\} \le C$. Here, $h_T := \operatorname{diam}(T)$ and $\rho(T) := \max\{r \mid B_r \subset T\}$ denotes the radius of the largest ball inscribed T.

3 Numerical approximation scheme

In order to solve (1)–(3) we use the following **semi-implicit linear approximation scheme:**

Let $n \in \mathbb{N}$, $\tau = \frac{T}{n}$, $0 < \tau \le 1/2$, $t_i = i\tau$ and $\sigma > 0$ be fixed numbers and u^0 be given by (3). *For $i = 1, \ldots n$, let $u^i \in V$ be the solution of*

$$\big(b'(u^{i-1})(u^i - u^{i-1}), v\big) + \tau(g(|\nabla G_\sigma * u^{i-1}|)\nabla u^i, \nabla v) = \tau(f(u^0 - u^{i-1}), v), \tag{12}$$

for all $v \in V$. These scale-discrete (u^i)'s are expected to be approximations of the image intensity function at the discrete scale instants t_i.

For the scale-discrete u^i's we state the following result.

Theorem 1. *For every $i = 1, \ldots, n$ there exists a unique solution u^i of* (12). *Moreover, there exists a positive constant C such that*

$$||u^i||_\infty \le C||u^0||_\infty.$$

The constant is given by $C = \mathrm{e}^{\left(2+\frac{L}{\gamma}\right)T}(1 + \frac{L}{\gamma})$. If $f \equiv 0$ then C can be chosen to be $C = 1$.

Proof. Our assertion is clearly true for u^0. Let it hold for u^{i-1}.

Due to (6), (7) and the Cauchy–Schwartz inequality we derive

$$|\nabla G_\sigma * u^{i-1}| \le D_\sigma < \infty,$$

and so there exists a constant ν_σ such that

$$g^{i-1} := g(|\nabla G_\sigma * u^{i-1}|) \ge \nu_\sigma > 0. \tag{13}$$

Thus, for any fixed σ, by the Lax–Milgram theorem and (9) we have existence and uniqueness of $u^i \in V$ which is the solution of (12). Moreover $u^i \in L_\infty(\Omega)$, see [14]. Thus the first part of the assertion is proved.

By the above conclusion we know that $v = u^i|u^i|^{p-1} \in V$ and we can use it as a test function in (12) for any $p \in \mathbb{N}$. Using (9) and (10) we obtain

$$\int_\Omega b'(u^{i-1})|u^i|^{p+1}dx + \tau\int_\Omega g^{i-1}p|u^i|^{p-1}|\nabla u^i|^2dx \le \int_\Omega b'(u^{i-1})|u^{i-1}||u^i|^p dx + L\tau\int_\Omega |u^0||u^i|^p dx + \frac{L}{\gamma}\tau \times \int_\Omega b'(u^{i-1})|u^{i-1}||u^i|^p dx.$$

Let us denote $C_1 = \frac{L}{\gamma}$. Then due to the positivity of the second term on the left hand side we have

$$\int_\Omega b'(u^{i-1})|u^i|^{p+1}dx \le (1 + C_1\tau)\int_\Omega b'(u^{i-1})|u^{i-1}||u^i|^p dx + L\tau\int_\Omega |u^0||u^i|^p dx. \tag{14}$$

Now we use Young's inequality in the form

$$ab \le \frac{1}{p+1}a^{p+1} + \frac{p}{p+1}b^{\frac{p+1}{p}}$$

in the last term of (14) with $a = \varepsilon|u^0|$, $b = \frac{1}{\varepsilon}|u^i|^p$. This together with (9) gives us

$$\int_\Omega b'(u^{i-1})|u^i|^{p+1}dx \le (1+C_1\tau)\int_\Omega b'(u^{i-1})|u^{i-1}||u^i|^p dx + L\tau\frac{\varepsilon^{p+1}}{p+1}\int_\Omega |u^0|^{p+1}dx + C_1\tau\frac{p}{p+1}\frac{1}{\varepsilon^{\frac{p+1}{p}}}\int_\Omega b'(u^{i-1})|u^i|^{p+1}dx.$$

Let us take $\varepsilon = \left(C_1\frac{p}{p+1}\right)^{\frac{p}{p+1}}$. Subtracting the last term we get

$$(1-\tau)\int_\Omega b'(u^{i-1})|u^i|^{p+1}dx \le (1+C_1\tau) \times \int_\Omega b'(u^{i-1})|u^{i-1}||u^i|^p dx + L\tau\frac{\varepsilon^{p+1}}{p+1}\int_\Omega |u^0|^{p+1}dx.$$

Since for $\tau \le \frac{1}{2}$ we have $\frac{1}{1-\tau} \le (1+2\tau)$ we obtain

$$\int_\Omega b'(u^{i-1})|u^i|^{p+1}dx \le (1+C_1\tau)(1+2\tau) \times \int_\Omega b'(u^{i-1})|u^{i-1}||u^i|^p dx + (1+2\tau)L\tau\frac{\varepsilon^{p+1}}{p+1} \times \int_\Omega |u^0|^{p+1}dx.$$

Let us use Young's inequality with $a = (1+C_1\tau)(1+2\tau)|u^{i-1}|$, $b = |u^i|^p$ in the first term on the right hand side and get

$$\int_\Omega b'(u^{i-1})|u^i|^{p+1}dx \le \frac{(1+C_1\tau)^{p+1}(1+2\tau)^{p+1}}{p+1} \times \int_\Omega b'(u^{i-1})|u^{i-1}|^{p+1}dx + \frac{p}{p+1} \times \int_\Omega b'(u^{i-1})|u^i|^{p+1}dx + (1+2\tau)L\tau\frac{\varepsilon^{p+1}}{p+1}\int_\Omega |u^0|^{p+1}dx.$$

Multiplying the previous inequality by $p+1$, subtracting the second term on the right hand side and using (9) we obtain the recurrent relation

$$\int_\Omega |u^i|^{p+1}dx \le (1+C_1\tau)^{p+1}(1+2\tau)^{p+1}\frac{\Gamma}{\gamma} \times \int_\Omega |u^{i-1}|^{p+1}dx + (1+2\tau)C_1\tau\varepsilon^{p+1}\int_\Omega |u^0|^{p+1}dx.$$

Then by the induction we get

$$\int_\Omega |u^i|^{p+1}dx \le (1+C_1\tau)^{i(p+1)}(1+2\tau)^{i(p+1)} \times \left(\frac{\Gamma}{\gamma}\right)^i (1+(1+2\tau)C_1T\varepsilon^{p+1})\int_\Omega |u^0|^{p+1}dx.$$

Taking the $(p+1)$-th root in the previous inequality and sending $p\to\infty$ (i is fixed and finite) we derive

$$||u^i||_\infty \le e^{(2+C_1)T}(1+C_1)||u^0||_\infty \le C||u^0||_\infty,$$

since $(1+x)^i \le e^{ix}$. Thus the assertion is proved with $C = e^{(2+C_1)T}(1+C_1)$ and $C_1 = \frac{L}{\gamma}$. Provided $f(s)\equiv 0$, a review of the arguments used above shows $C=1$ without any restriction on the time step τ. ∎

The image may be understood as a piecewise linear function interpolating the given discrete values of the image intensity function. The centers of the image voxels then correspond in a natural way to the nodes of a finite element grid. Such an approach is natural for a discretization with piecewise linear finite elements, see below.

As the smoothing kernel in (1) we use the Gauss function

$$G_\sigma(x) = \frac{1}{(2\sqrt{\pi\sigma})^d}e^{-\frac{|x|^2}{4\sigma}} \tag{15}$$

with a given positive σ. In that case the term $\nabla G_\sigma * u^{i-1}$ in (12) represents the gradient of the solution at time σ of the linear heat equation in $\mathbb{R}^3$ with initial condition given by the extension (e.g. by reflection) of u^{i-1}. Using that idea, we replace the convolution term in (12) by solving implicitly the linear heat equation with reflective (homogeneous Neumann) boundary conditions with just one time discretization step with length σ. Thus, we end up with the following system of equations, semi-implicit in scale:

$$(b'(u^{i-1})u^i, v) + \tau(g(|\nabla u^c|)\nabla u^i, \nabla v) = (b'(u^{i-1})u^{i-1} + \tau f(u^0 - u^{i-1}), v) \tag{16}$$

where $u^c \in V$ replaces the convolution $G_\sigma * u^{i-1}$ and is the solution of the problem

$$(u^c, v) + \sigma(\nabla u^c, \nabla v) = (u^{i-1}, v). \tag{17}$$

The weak identities (16)–(17) are starting points to derive a fully discrete semi-implicit finite element discretization of (1)–(3). To that goal the variational identities (16)–(17) are projected to finite dimensional subspaces consisting of piecewise linear finite elements $V_h \subset V$, $V_h = V_h(\mathcal{T}_i) := \{v_h \in C^0(\bar\Omega) | v_{h|T} \in \mathcal{P}_1 \text{ for all } T \in \mathcal{T}_i\}$, where $\mathcal{P}_1$ denotes the set of linear polynomials and $\mathcal{T}_i$ is a conforming triangulation of $\Omega \subseteq \mathbb{R}^3$ at the i-th discrete scale step. By introducing the Lagrangian bases of hat functions $\varphi_j \in V_h(\mathcal{T}_i)$, determined by $\varphi_j(x_k) = \delta_{j,k}$ for all vertices x_k, $k = 1, \dots N_i$ of $\mathcal{T}_i$, N the number of vertices, a function $v_h \in V_h$ is given by $v_h = \sum_{k=1}^N v_k\varphi_k = \sum_{k=1}^N v_h(x_k)\varphi_k$.

For each discrete scale instant $i = 1, \dots n$ we are looking for a function $u_h^i \in V_h(\mathcal{T}_i)$ fulfilling

$$(b'(u_h^{i-1}); u_h^i, v_h)_h + \tau(g(|\nabla u_h^c|)\nabla u_h^i, \nabla v_h) = (b'(u_h^{i-1}); u_h^{i-1}, v_h)_h + \tau(\mathbb{1}; f(u_0 - u_h^{i-1}), v_h)_h \tag{18}$$

for all $v_h \in V_h(\mathcal{T}_i)$ where $u_h^c \in V_h(\mathcal{T}_i)$ is the solution of

$$(\mathbb{1}; u_h^c, v_h)_h + \sigma(\nabla u_h^c, \nabla v_h) = (\mathbb{1}; u_h^{i-1}, v_h)_h \quad \forall v_h \in V_h(\mathcal{T}_i), \tag{19}$$

where $(w; u_h, v_h)_h$ is the lumped L^2 inner product, defined by

$$(w; u_h, v_h)_h := \sum_k w(x_k) u_h(x_k) v_h(x_k) \int_\Omega \varphi_k.$$

Using the above bases representation (18)–(19) may be written in the form

$$\sum_{k=1}^{N} \Big\{ (b'(u_h^{i-1}); \varphi_k, \varphi_j)_h + \tau(g(|\nabla u_h^c|)\nabla\varphi_k, \nabla\varphi_j) \Big\} u_k^i =$$
$$(b'(u_h^{i-1}); u_h^{i-1}, \varphi_j)_h + \tau(\mathbb{1}; f(u_0 - u_h^{i-1}), \varphi_j)_h$$

and

$$\sum_{k=1}^{N} \Big\{ (\mathbb{1}; \varphi_k, \varphi_j)_h + \sigma(\nabla\varphi_k, \nabla\varphi_j) \Big\} u_k^c = (\mathbb{1}; u_h^{i-1}, \varphi_j)_h$$

for all $j = 1, \ldots N$.

Thus solving (18)–(19) means inverting two linear systems with matrices

$$\mathbf{M}\left(b'(u_h^{i-1})\right) + \tau\mathbf{A}(g(|\nabla u_h^c|)),$$
$$\mathbf{M}(\mathbb{1}) + \sigma\mathbf{A}(\mathbb{1}),$$

with $\mathbf{M}_{j,k}(w) = (w; \varphi_k, \varphi_j)_h$ the lumped mass matrix and $\mathbf{A}(w)_{j,k} = (w\nabla\varphi_k, \nabla\varphi_j)$ the stiffness matrix.

4 Multiscale image coarsening

As mentioned above, we use a coarsening strategy for the finite element meshes to increase the effectiveness of the procedure. Since the image is being smoothed as scale evolves, and by analogy with the result of [12], we do not expect a movement of the main edges, (local) coarsening is an appropriate way to decrease the number of unknowns.

To be more precise we proceed as follows. We generate a triangulation $\mathcal{T}_0$ corresponding to a voxel structure of the image by (globally) refining a coarse grid $\mathcal{T}^0$, the so called *macro triangulation*. We choose the *bisection method*, which allows for coarsening quite easily and was introduced for the 3D case in [3]. This refinement procedure generates a sequence $\mathcal{T}^0, \mathcal{T}^1, \mathcal{T}^2, \ldots$ of finer and finer meshes until the desired (initial) mesh size is reached.

During time-scale evolution, in every time step local coarsening is used to reduce the number of unknowns according to a certain coarsening criterion, see below.

We briefly recall the bisection method, for further details see [3]:

4.1 Refinement by bisection

Consider a tetrahedron $T \in \mathcal{T}^0$, which has been cut open along the three edges which meet at vertex P_4 and unfolded:

With each of the four triangular faces of T we associate a *refinement edge* (one example is shown in Fig. 1). We make the following assumptions:

(A1) For each tetrahedron there is at least one common refinement edge for two different faces of the tetrahedron adjacent to this edge ($\overline{P_{i_1} P_{i_3}}$ in Fig. 1). We call such an edge a *global refinement edge* of the tetrahedron.

(A2) If T_1, T_2 are two tetrahedra with $T_1 \cap T_2 = S$ and S is a triangle, then the refinement edge of S with respect to T_1 and the refinement edge of S with respect to T_2 is the same.

Note that assumptions (A1) and (A2) can be fulfilled for an arbitrary conforming triangulation: There is an ordering of the edges of a triangulation (for instance in terms of their lengths). Choose the refinement edge of a triangular face as the one with highest index corresponding to this ordering. Then (A1) and (A2) are fulfilled.

Let us first consider the split of a single tetrahedron:

A single tetrahedron is bisected by cutting through the midpoint of the global refinement edge to the opposite vertices, thus introducing the midpoint as a new node P_{new}. We get two new tetrahedra:

The refinement edges of the bisected triangles are chosen as indicated by Fig. 2. Here, $*$ indicates an arbitrary position of the refinement edge which is not affected by the split. The question then is, how to choose the refinement edge for the new triangle $P_{new} P_4 P_3$. One requirement is of course the condition that both new tetrahedra must have again a global refinement edge.

In [3] it is outlined how to choose this refinement edge properly. The above procedure is the atomic operation to split a single element. For the global situation the following algorithm is used.

Bisection algorithm:
Let $\mathcal{T}^k$ be a given triangulation, either $k = 0$ or $\mathcal{T}^k$ being a refinement of $\mathcal{T}^{k-1}$. Let $\Sigma^+ \subseteq \mathcal{T}^k$ be a set of tetrahedra to be divided.

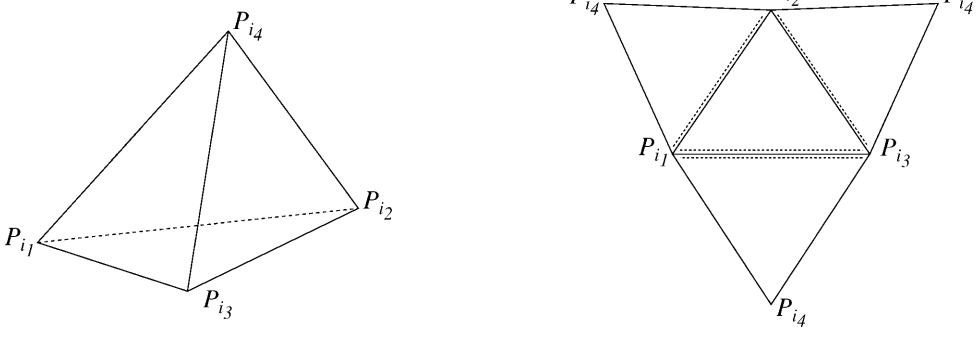

Fig. 1. Tetrahedron; dashed lines indicate the refinement edges

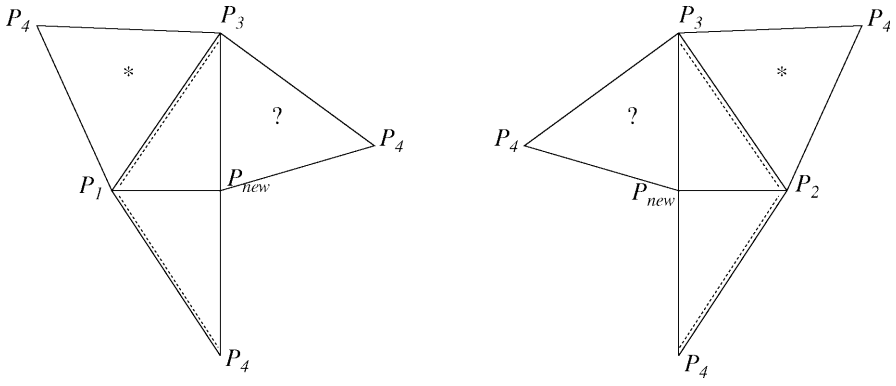

Fig. 2. Bisection of a single tet

while $\Sigma^+ \neq \emptyset$ **do**

bisect all $T \in \Sigma^+$ as described above, obtain the intermediate triangulation $\hat{\mathcal{T}}^k$ (possibly non-conforming)

let now Σ^+ be the set of those tetrahedra with a non-conforming node.

endwhile

$\mathcal{T}^{k+1} := \hat{\mathcal{T}}^k$

In [3] the following is shown:

Theorem 2. Let the conforming triangulation $\mathcal{T}^k$ fulfill assumptions (A1) and (A2). Then the above algorithm stops in a finite number of steps and $\mathcal{T}^{k+1}$ is conforming. The sequence $\mathcal{T}^0, \mathcal{T}^1, \mathcal{T}^2, \ldots$ is shape regular.

4.2 Local coarsening

We choose the bisection method to generate the starting triangulation $\mathcal{T}_0$ because a triangulation which was derived by a successive application of bisection steps can be derefined very easily. We make the following definitions:

Definition:

i.) A tet $T \in \mathcal{T}$ has level l if T was obtained after l refinement steps.

ii.) A tet T is said to have *locally finest level* if the levels of all neighbors are less than or equal to the level of T.

iii.) Let $T \in \mathcal{T}$ and let T' be the father of T. A vertex P of T which was inserted while bisecting T' is called the *coarsening node* of T.

iv.) Let K be an edge of the triangulation $\mathcal{T}$ and K' the "father"-edge of K with midpoint Q. Set $M := \{T \in \mathcal{T} \,|\, T \cap K' \neq \emptyset\}$. If Q is the coarsening node for all $T \in M$ then M is called a *resolvable patch*.

Figure 3 shows a resolvable patch and the coarsened patch.

If M is a resolvable patch, then all $T \in M$ can be coarsened without interfering with $T' \in \mathcal{T}$ outside of M. Therefore resolvable patches are the configurations which we allow to be coarsened. This guarantees that the coarsening process stays local.

We may write the coarsening algorithm in the following form:

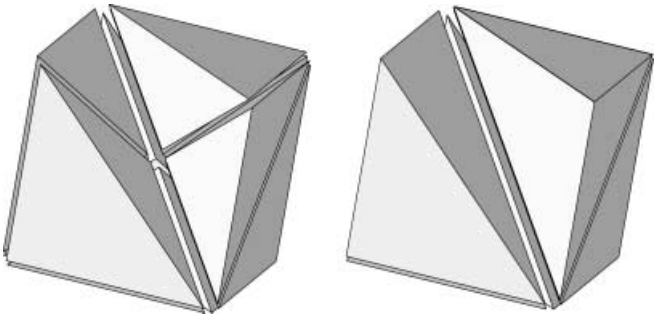

Fig. 3. Resolvable patch and coarsened patch

Coarsening algorithm:
Let $\mathcal{T}^i$ be a triangulation obtained by refinement and coarsening steps. Let $\Sigma^- \subset \mathcal{T}^i$ be the set of tetrahedra to be derefined. Then one coarsening step consists of:

for each $T \in \Sigma^-$ **do**
  if T belongs to a resolvable patch M **then**
    if $T' \in \Sigma^-$ for all $T' \in M$ **then**
      derefine M, see Fig. 3
    endif
  endif
enddo

Since we only derefine resolvable patches the question arises whether there are "enough" resolvable patches in an arbitrary triangulation. In [5] it is shown that at least for so–called "standard triangulations" the following holds: All tetrahedra of locally finest levels belong to resolvable patches. This means that using the above algorithm a total derefinement of a triangulation is possible.

4.3 Coarsening criterion and adaptive method

As the local behavior of ∇u determines the evolution process and is an indicator for edges, the coarsening criterion is based on this value. More precisely, let $\epsilon > 0$ be a given tolerance. For i a time-scale step and u_h^i the corresponding numerical solution on the grid $\mathcal{T}_i$ we allow all tetrahedra $T \in \mathcal{T}_i$ to be coarsened, if

$$h_T |\nabla u_h^i| \leq \epsilon \quad \text{on } T. \tag{20}$$

Note that since u_h^i is piecewise linear, ∇u_h^i is constant on each tetrahedron.

Thus we have the following adaptive scheme to approximate (1)–(3):

Let $\mathcal{T}_0, u_0$ be given.

for $i = 1, 2, \ldots n$ **do**
  define $\Sigma^- := \{T \in \mathcal{T}_{i-1} \mid h_T |\nabla u_h^{i-1}| \le \epsilon \text{ on } T\}$
  derefine $\mathcal{T}_{i-1}$ according to Σ^- to obtain $\mathcal{T}_i$
  set up the matrix $\mathbf{M}(\mathbb{1}) + \sigma \mathbf{A}(\mathbb{1})$
  compute $u_h^c \in V_h(\mathcal{T}_i)$ solving (19)
  set up the matrix $\mathbf{M}(b'(u_h^{i-1})) + \tau \mathbf{A}(g(|\nabla u_h^c|))$
  compute $u_h^i \in V_h(\mathcal{T}_i)$ solving (18)
enddo

5 Numerical experiments

In this Section we present two numerical examples computed by the scheme (18)–(19) using the 3D coarsening strategy. In the computations we used the following definition for g:

$$g(s) = \frac{1}{1 + Ks^2},$$

where $K > 0$ is a constant. This Perona–Malik form of g is well suited for image selective smoothing. However, also other non-trivial modifications are available in the literature, see e.g. [7]. The right hand side f was set $f \equiv 0$ in the presented computations. A linear f gives comparable results.

In the first example we consider an artificial image containing the object visualized in Fig. 5. The surface S of this object is described by the equation

$$S := \left\{ x = (x_1, x_2, x_3) \mid r = 0.475 * \left| 3\left(\frac{x_2}{r}\right)^2 - 1 \right|,\ r = |x| \right\}.$$

Note that this object is smooth (up to singular lines) and the "steps" in Fig. 5 are due to the resolution of the triangulation. The initial function takes values $u^0 = 0.6$ inside and $u^0 = 0.5$ outside the object, respectively, plus additive random noise with range $[-0.15, 0.15]$. The object boundary has large variations of curvature and the level of noise is high in comparison with the un-noisy difference in intensity. The computational results in this example are presented in Figs. 6–9 and in Table 1. In Fig. 6 we present successive 3D filtering visualizing level surfaces until the desired object is extracted. In Fig. 7 we plot 2D slices to show how the original intensity is corrupted by noise and how the noise is filtered out. From both Figures, one can see that object boundaries are preserved very well while noise is removed at the same time.

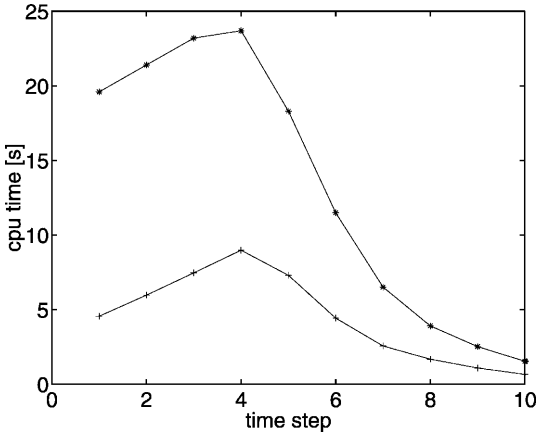

Fig. 4. Overall cpu time (∗) and cpu time for mesh adaptation (+), respectively, on a Compaq ES40 with 500 MHz, example 1

Fig. 5. Original artificial image without noise

In Figs. 8 and 9 we plot the results of scaling together with a cut of the computational tetrahedral grid in order to illustrate the local coarsening. In this example we took $b(s) = s$, $K = 5$. Table 1 shows the decrease in the number of degrees of freedom due to coarsening. Figure 4 document the overall cpu time and the cpu time devoted to mesh adaptation.

Next, we have applied our method to a real image representing an *in vivo* acquired 3D echo-cardiography. The acquisition represents a certain time instant of the cardiac cycle of a real patient. In Fig. 11 the isosurface corresponding to the interface between the cardiac muscle and blood is visualized using an original echo-image (top left) and after processing by our algorithm. We took advantage of the fact that the grey value describing this interface is known by setting

$$b(s) = \begin{cases} s & \text{for} \quad s \le s^*, \\ 10^{-3}s + s^* & \text{for} \quad s > s^*, \end{cases}$$

Table 1. Decrease of number of unknowns, example 1

time step	0	1	2	3	4	5	6	7	8	9	10
♯ unknowns	274 625	274 623	274 554	272 206	249 774	198 105	134 561	77 670	49 173	35 458	24 930

Table 2. Decrease of number of unknowns, example 2

time step	0	1	2	3	4	5	6	7	8
♯ unknowns	274 625	178 777	158 355	132 335	110 617	95 619	85 190	77 525	71 906

where s^* is sufficiently larger than the level of this isosurface, $K = 5$. Table 2 gives again the number of nodes in subsequent triangulations and Fig. 10 shows the cpu times in this example.

We note that even if we do not have a theoretical analogy of the semi-discrete stability estimate (Theorem 1) for our fully discrete scheme, we do not observe any L^∞ instabilities in the computations.

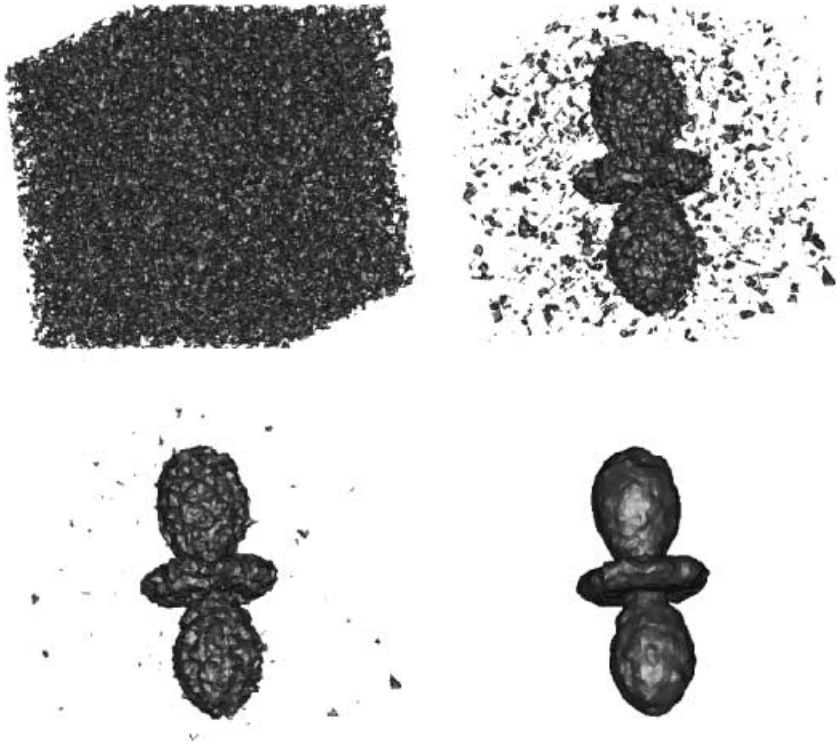

Fig. 6. Smoothing of the artificial image. Visualization of the 0th, 3rd, 6th and 10th time-scale step

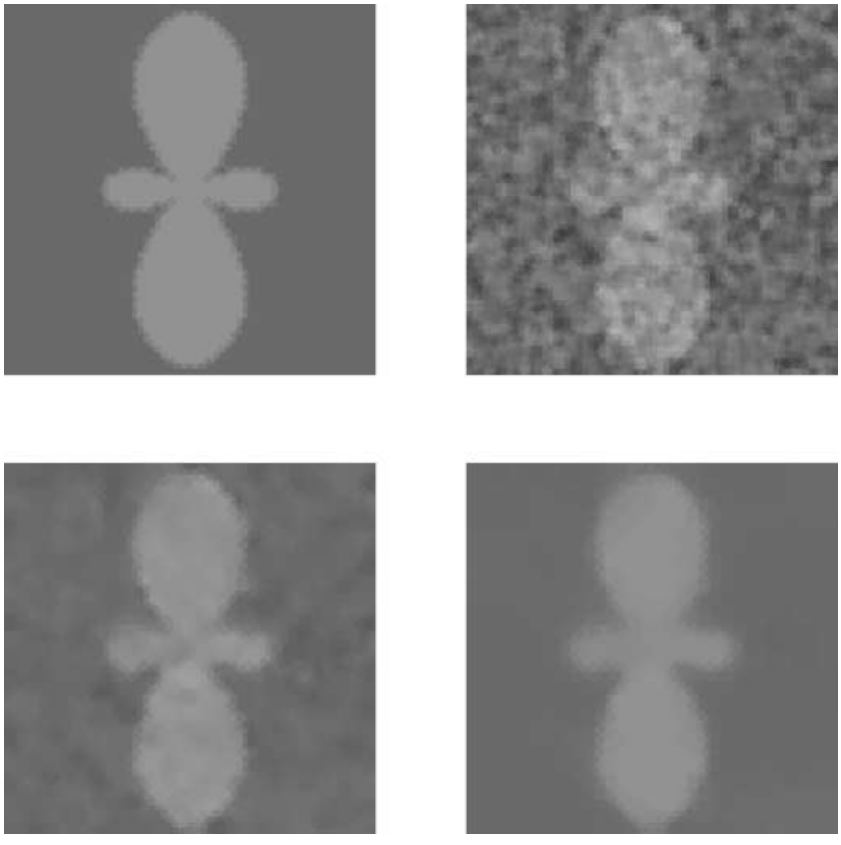

Fig. 7. Smoothing of the artificial image, 2D slices at $x_3 = 0$. Cut of un-noisy original (*top left*), cut of noise-corrupted initial image (*top right*) and filtering after 4 (*bottom left*) and 10 (*bottom right*) time-scale steps, respectively

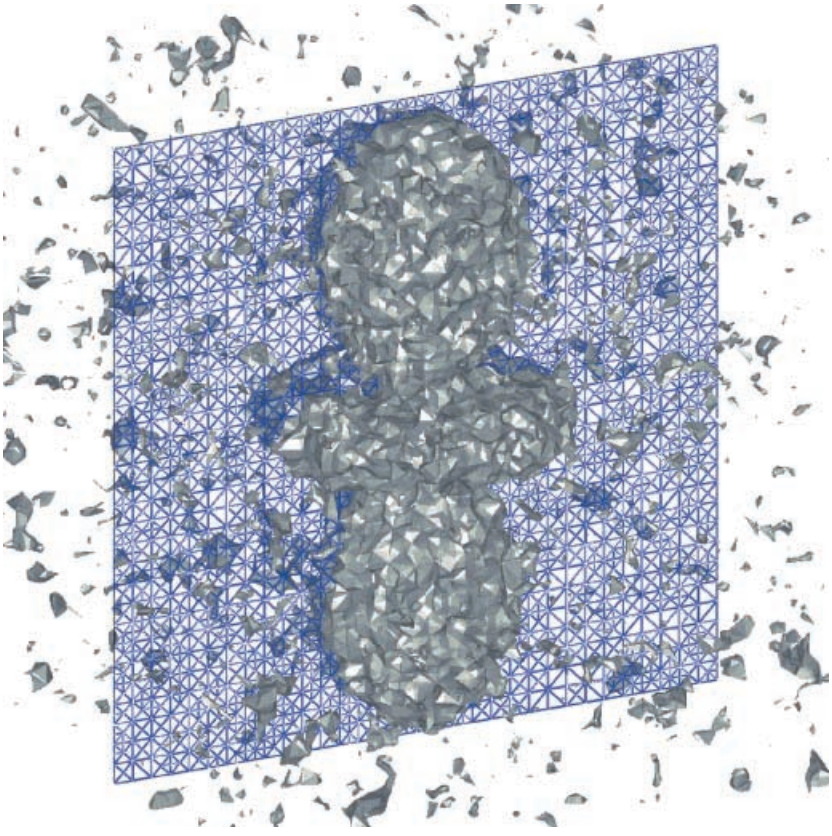

Fig. 8. Level surface and computational grid at the 4th scale step

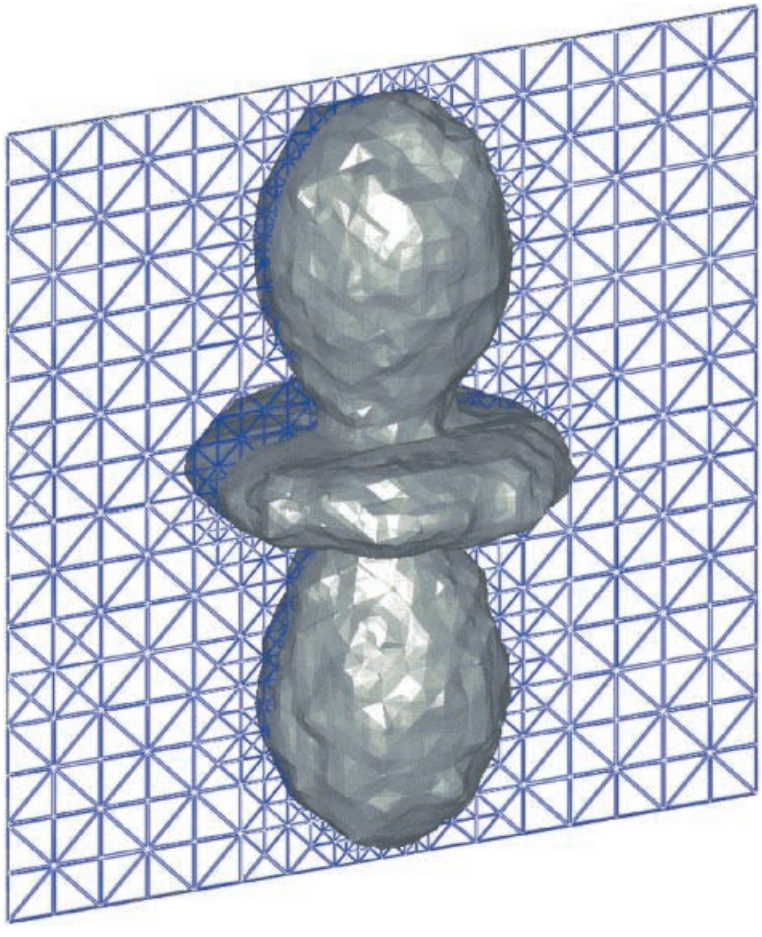

Fig. 9. Level surface and computational grid at the 10th scale step

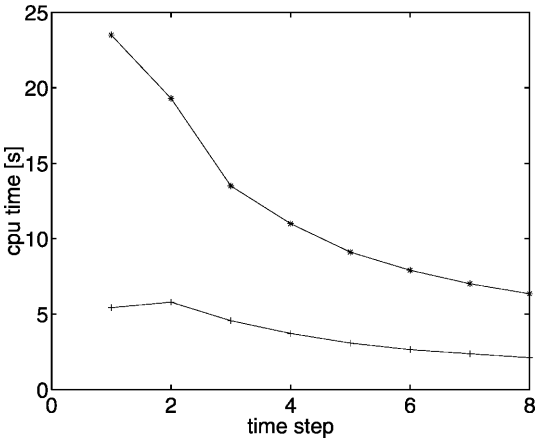

Fig. 10. Overall cpu time (∗) and cpu time for mesh adaptation (+), respectively, on a Compaq ES40 with 500 MHz, example 2

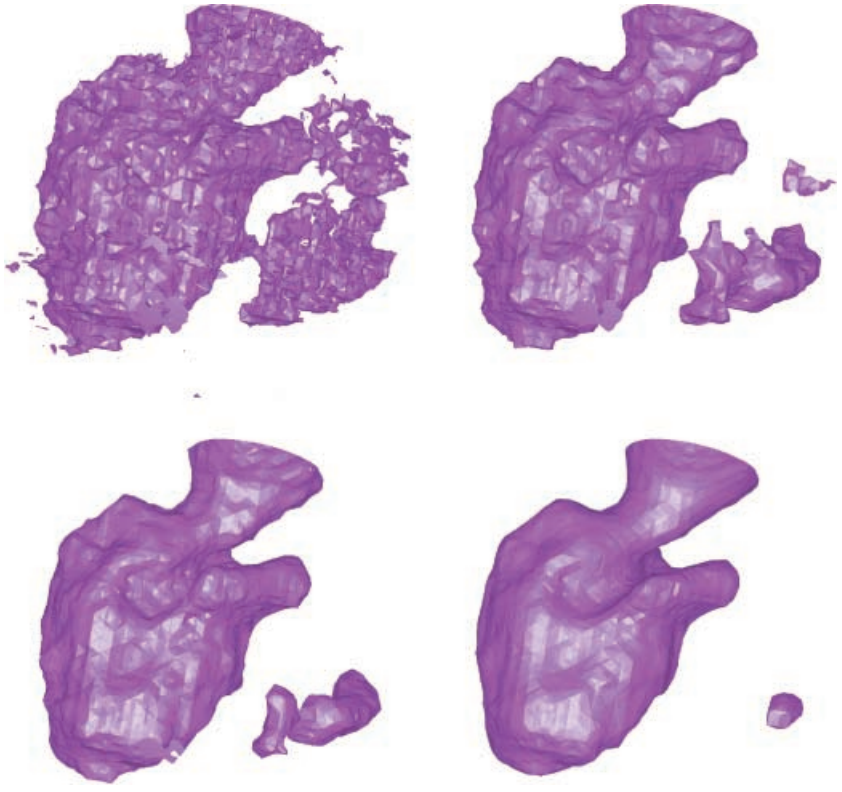

Fig. 11. Smoothing of the human left ventricle. Visualization of the corresponding level surfaces at the 0th, 2nd, 4th and 8th scale steps respectively

Acknowledgements. We would like to thank Prof. Claudio Lamberti and Dr. Alessandro Sarti from the University of Bologna for providing the TomTec 3D echocardiographic data.

References

1. Alvarez, L., Guichard, F., Lions, P.L., Morel, J.M.: Axioms and Fundamental Equations of Image Processing. Archive for Rat. Mech. Anal. 123, 200–257 (1993)
2. Alvarez, L., Lions P.L., Morel, J.M.: Image selective smoothing and edge detection by nonlinear diffusion II. SIAM J. Numer. Anal. 29, 845–866 (1992)
3. Bänsch, E.: Local Mesh Refinement in 2 and 3 Dimensions. IMPACT of Computing in Science and Engineering 3, 181–191 (1991)
4. Bänsch, E.: Adaptive Finite–Element Techniques for Navier–Stokes Equations and other Transient Problems. In: Adaptive Finite and Boundary Elements. Computational Mechanics Publications and Elsevier 1993
5. Bänsch, E.: Mesh refinement in two and three dimensions. In: INRIA course "Calcul d'erreur a posteriori et adaptation de maillage". Rocquencourt (France) 9/1995
6. Bänsch, E., Mikula, K.: A coarsening finite element strategy in image selective smoothing. Computing and Visualization in Science 1, 53–61 (1997)
7. Black, M.J., Sapiro, G., Marimont, D., Heeger, D.: Robust anisotropic diffusion. IEEE Transactions on Image Processing 7(3), 421–432 (1998)
8. Caselles, V., Morel, J.-M., Sapiro, G., Tannenbaum, A. (eds.): Special issue on partial differential equations and geometry-driven diffusion in image processing and analysis. IEEE Transactions on Image Processing 7(3) (1998)
9. Catté, F., Lions, P.L., Morel, J.M., Coll, T.: Image selective smoothing and edge detection by nonlinear diffusion. SIAM J. Numer. Anal. 29, 182–193 (1992)

10. Kačur, J., Mikula, K.: Solution of nonlinear diffusion appearing in image smoothing and edge detection. Applied Numerical Mathematics 17, 47–59 (1995)
11. Kačur, J., Mikula, K.: Slow and fast diffusion effects in image processing. Comput. Visual. Sci. 3, 185–195 (2001)
12. Kawohl, B., Kutev, N.: Maximum and comparison principle for one-dimensional anisotropic diffusion. Math. Ann. 311, 107–123 (1998)
13. Koenderink, J.J.: The structure of images. Biol. Cybern. 50, 363–370 (1984)
14. Ladyzenskaja, O.A., Uralceva, N.N.: Linear and Quasilinear elliptic equations. Academic Press 1968
15. Nitzberg, M., Shiota, T.: Nonlinear image filtering with edge and corner enhancement. IEEE Trans. Pattern Anal. Mach. Intel. 14, 826–833 (1992)
16. Osher, S., Rudin, L.: Feature oriented image enhancement using shock filters, SIAM J. Numer. Anal. 27, 919–940 (1990)
17. Perona, P., Malik, J.: Scale space and edge detection using anisotropic diffusion. In Proc. IEEE Computer Society Workshop on Computer Vision (Miami Beach, Nov. 30–Dec.2, 1987). Washington: IEEE Computer Society Press, 16–22 (1987)
18. Preusser, T., Rumpf, M.: An adaptive finite element method for large scale image processing. Journal for Visual Communication and Image Representation 11(2), 183–195 (2000)
19. ter Haar Romeny, B.M. (ed.): Geometry driven diffusion in computer vision. Dodrecht: Kluwer 1994
20. Serra, J.: Image analysis and mathematical morphology. New York: Academic Press 1982
21. Weickert, J., Ishikawa, S., Imiya, A.: Scale space has been discovered in Japan. J. Math. Imaging Vision 10, 237–252 (1999)
22. Witkin, A.P.: Scale-space filtering. Proc. Eight Int. Conference on Artificial Intelligence 2, 1019–1022 (1983)